RSC Advances

PAPER



Cite this: *RSC Adv.*, 2020, **10**, 1883

# Site-selective doping effect, phase separation, and structure evolution in 1:1:1 triple-cation B-site ordered perovskites $Ca_{4-x}Sr_xGaNbO_8$†

He Huang,[a] Pengfei Jiang, *[ab] Wenliang Gao,[a] Rihong Cong[a] and Tao Yang *[a]

Received 28th November 2019
Accepted 30th December 2019

DOI: 10.1039/c9ra09970k

rsc.li/rsc-advances

Oxygen-deficient perovskites are a family of important materials that may exhibit oxide ionic conductivities. We attempted to introduce oxygen-vacancy disordering in perovskite $Ca_4GaNbO_8$ ($Ca_4$-type) by substituting $Ca^{2+}$ with larger $Sr^{2+}$. $Sr^{2+}$-to-$Ca^{2+}$ substitution did not lead to oxygen-vacancy ordering–disordering transition but an interesting $Ca_4$-to-$Sr_4$ type structure transition. Rietveld refinements revealed that the two-type structures exhibit similar oxygen-vacancy ordering and identical 1:1:1 triple-cation B-site ordering. Close inspection of the two-type structures revealed the subtle structure difference lies in the orientations of $GaO_4$ tetrahedra, which is the origin of the formation of the narrow two-phase region ($0.3 \leq x < 0.65$) in $Ca_{4-x}Sr_xGaNbO_8$. More importantly, the A- and B-site cavities with large differences in size for both structures resulted in a site-selective doping behaviour for $Sr^{2+}$ in $Ca_{4-x}Sr_xGaNbO_8$. These structural changes found in $Ca_{4-x}Sr_xGaNbO_8$ will provide a broad route approaching new oxygen-deficient phases with oxide ionic conductivities.

## Introduction

Perovskites with the general formula $ABO_3$ can accommodate cations with a wide range of ionic radii and charge, thus giving rise to rich chemical compositions accompanied with diverse physical properties such as magnetism,[1,2] superconductivity,[3,4] dielectricity,[5,6] ferroelectric.[7–9] Such diversity in chemical compositions as well as physical properties for perovskites have motivated an intense and enduring interesting for chemists to design new materials and modify the physical properties of a specific phase by chemical substitution.

Among the various perovskites, 1:1 double-cation B-site ordering perovskites usually exhibit physical properties different from the disordered ones distinctively. For example, B-site ordered perovskites $Sr_2FeMoO_6$ and $Sr_2CrOsO_6$ exhibit colossal magnetoresistance and high temperature ferrimagnetism, respectively.[10,11] In perovskites, B-site rock-salt ordering is commonly observed, because such an arrangement manner of B-site cations is benefit for keeping local charge neutrality and release of structure strain. In contrast, the layered ordered and columnar ordered perovskites are relatively rare, and only a few specific phases have been reported up to now.[12,13]

Owing to the structural flexibility, perovskite can accommodate various defects including A-site and oxygen vacancies, which can result in ionic diffusion at high temperature. A-site ionic diffusion was observed indeed in $Li_{3x}La_{2/3-x}TiO_3$, in which the pre-existing A-site vacancies allow for easy $Li^+$ diffusion.[14–16] In contrast to A-site ionic conductivity, oxygen ionic conductivity or mixed ionic and electronic conductivities for oxygen deficient perovskites are much more widely investigated due to their potential applications in solid oxide fuel cells (SOFCs) as electrolyte or cathode. For example, $Sr^{2+}$ and $Mg^{2+}$ co-doped $LaGaO_3$ (LSGM) is the one of the best oxygen ionic conducting electrolytes.[17–19] Much efforts have been devoted to improve the oxygen ionic conductivities of various perovskites by increasing the number of oxygen vacancies. However, increasing the number of oxygen vacancies may result in completely ordering of oxygen vacancies, which in turn lead to a significant decrease of oxide ionic conductivity. For example, oxygen-vacancy ordered perovskite $Ba_2In_2O_5$ exhibits poor ionic conductivity in low temperature range (<900 °C), though there exists a large number of oxygen vacancies in the structure.[20–22] Oxygen-vacancy ordering/disordering in perovskite is closely related to the A-site cationic size (or tolerance factor, $t$). For example, with an increase of the $Sr^{2+}$-content (increase of tolerance factor) in $Ca_{2-x}Sr_xFeCoO_{6-\delta}$ resulted in an oxygen-vacancy ordering to disordering transition.[23] Therefore, the strategy of increasing the A-site cationic size of anion-ordered perovskites might be utilized to improve the oxide ionic conductivity.

Herein this contribution, our attention is turned to the newly discovered oxygen-deficient perovskite $Ca_4GaNbO_8$, where the

[a]College of Chemistry and Chemical Engineering, Chongqing University, Chongqing, 401331, P. R. China. E-mail: pengfeijiang@cqu.edu.cn; taoyang@cqu.edu.cn
[b]College of Physics, Chongqing University, Chongqing, 401331, P. R. China

† Electronic supplementary information (ESI) available: Rietveld refinement patterns, crystallographic parameters, selected interatomic distances for $Ca_{4-x}Sr_xGaNbO_8$ ($x = 0$, 1, 1.5, 2, 2.5, 3, 3.5, and 4). See DOI: 10.1039/c9ra09970k

complex 1:1:1 triple-cation B-site ordering is coupled with the oxygen-deficient ordering.[24] We attempted to incorporate larger $Sr^{2+}$ cations into $Ca_4GaNbO_8$ to bring in oxygen-vacancy disordering, so as to obtain new oxide ionic conductors. Substitution of $Ca^{2+}$ with $Sr^{2+}$ led to a $Ca_4$-type to the $Sr_4$-type structure transition as we expected. Unfortunately, Rietveld refinements manifested that the oxygen vacancies are also ordered in the $Sr_4$-type structure, which was further confirmed by AC impedance spectroscopy measurements on selected compositions due to the absence of oxide ionic conductivity. The subtle structural differences between the $Ca_4$-and $Sr_4$-type structures lie in the orientations of $GaO_4$ tetrahedra, which is the origin of the coexistence of two phases in a narrow region $0.3 \leq x < 0.65$. Moreover, a site-selective doping behaviour was observed for $Sr^{2+}$ in $Ca_{4-x}Sr_xGaNbO_8$, however the A-site cationic ordering is only in short-range for all compositions.

## Experimental section

### Synthesis

The polycrystalline samples $Ca_{4-x}Sr_xGaNbO_8$ ($x$ = 0–4) were prepared by high temperature solid-state reactions using calcium carbonate ($CaCO_3$, 99.99%), strontium carbonate ($SrCO_3$, 99.99%), gallium oxide ($Ga_2O_3$, 99.99%), niobium oxide ($Nb_2O_5$, 99.99%) as raw materials. The starting materials were preheated at 500 °C for 10 h to remove the absorbed moisture. Stoichiometric starting materials with a total weight of 1.2 g were weighted and mixed in an agate mortar by hands and then preheated at 950 °C to decompose the carbonates. After this calcination, the resultant white powders were further grinded and pressed into pellet with 13 mm diameter and then calcinated between 1200 °C and 1300 °C for 60 hours with intermediate grinding and pressing.

### X-ray diffraction

The phase purity of the samples was investigated by powder X-ray diffraction (PXRD). PXRD were performed on the PANalytical Empyrean diffractometer equipped with a PXIcel 1D detector (Cu Kα radiation). The operation voltage and current were 40 kV and 40 mA, respectively. The PXRD data for phase identification were collected with the setting of 30 s/0.0262°. High quality PXRD data, which were used for Rietveld refinements with the TOPAS-Academic V6 software,[25] were collected with a setting of 200 s/0.0131°.

### AC impedance spectroscopy

AC impedance spectroscopy measurements for $Ca_{4-x}Sr_x$-$GaNbO_8$ ($x$ = 0, 2, and 4) were carried out over temperature range from room temperature to 800 °C using a Solartron 1260A impedance phase analyzer with the frequency from $10^{-1}$ to $10^7$ Hz. Before the measurements, the pellets were coated with platinum pasts and then heated at 800 °C for 1 h to form electrodes.

### Raman spectroscopy

The Raman spectroscopy measurements were performed on the LabRAM HR Evolution spectrometer. The room temperature Raman spectra for $Ca_4GaNbO_8$ and $Sr_4GaNbO_8$ were measured over the range of 100–4000 $cm^{-1}$ using the 325 nm line and with the light focus on the sample trough an optical lens. The spectral resolution was about 1–2 $cm^{-1}$.

## Results and discussion

### Phase identification

PXRD data for $Ca_{4-x}Sr_xGaNbO_8$ ($x$ = 0–4) are elucidated in Fig. 1, where the diffraction peaks continuous evolves to lower angles upon increasing $Sr^{2+}$-content. This observation indicates the cell volume expansion of $Ca_{4-x}Sr_xGaNbO_8$ upon substituting $Ca^{2+}$ with $Sr^{2+}$, which is consistent with the larger cationic radii of $Sr^{2+}$ (1.44 Å in 12-fold coordination) in comparison with $Ca^{2+}$ (1.34 Å in 12-fold coordination).[26]

Previous study on $Ca_4GaNbO_8$ revealed that this compound adopts a triple-cation B-site ordered perovskite-type structure and crystallizes in $P2_1/c$ with lattice parameters $a \approx 11.18$ Å,

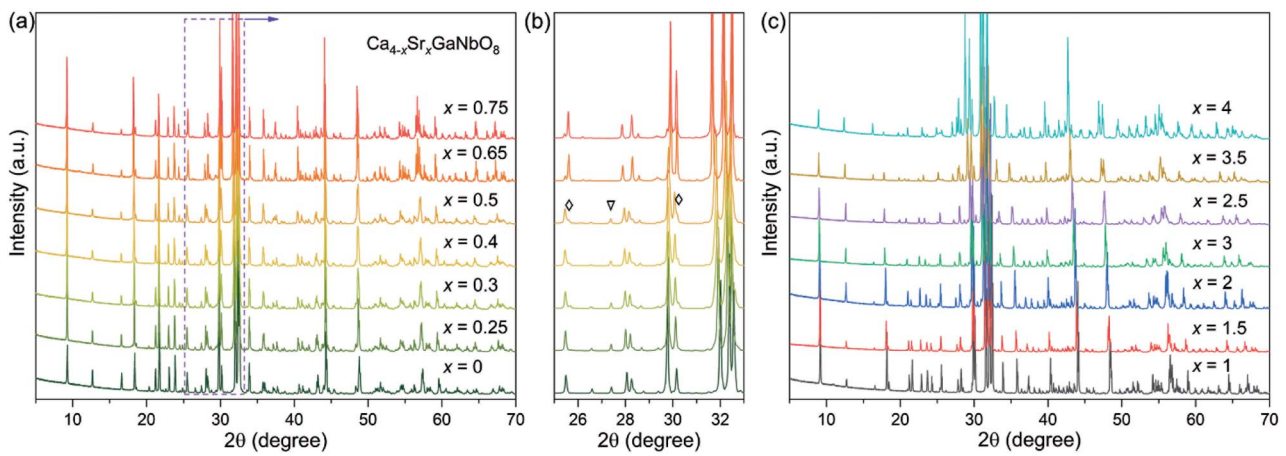


Fig. 1 (a and c) Powder XRD patterns for $Ca_{4-x}Sr_xGaNbO_8$ ($x$ = 0–4). (b) The enlargement of 25–33° range for compositions $x \leq 0.65$. The triangle represents the specific reflection ascribe to $Ca_4$-type phase, the diamonds represent the reflections ascribe to $Sr_4$-type phase.

$b \approx 5.59$ Å, $c \approx 14.07$ Å, and $\beta \approx 121.55°$.[24] Our preliminary Le-bail fitting performed on $Ca_{4-x}Sr_xGaNbO_8$ manifested that the XRD data for compositions with $x < 0.65$ could be indexed by this monoclinic cell. However, a group of weak reflections for compositions with $x \geq 0.65$, which is not ascribe to impurity phases, could not be fitted with this monoclinic cell any more, indicating $Sr^{2+}$-doping induced a change of lattice parameters. Indexing the XRD data of $Ca_3SrGaNbO_8$ yield a monoclinic cell with lattice parameters $a \approx c_1/2$, $b \approx b_1$, $c \approx \sqrt{3}a_1$, $\beta \approx 97°$, where $a_1$, $b_1$, and $c_1$ represent the cell dimension of $Ca_4GaNbO_8$ (denoted as $Ca_4$-type phase). Similar unit cell was also observed for $Sr_4AlNbO_8$ ($P2_1/c$), which also adopt a triple-cation B-site ordered perovskite-type structure with anionic vacancy ordering, suggesting $Ca_{4-x}Sr_xGaNbO_8$ ($x \geq 0.65$) (denoted as $Sr_4$-type phase) is isostructural to $Sr_4AlNbO_8$.[27]

Preliminary Rietveld refinements performed on $Ca_{4-x}Sr_x$-$GaNbO_8$ ($x = 0.5$) using $Ca_4GaNbO_8$ as the initial structure model resulted in unreasonable structural parameters, *i.e.* too short interatomic distances. Close inspection of the XRD data revealed that some reflections from the $Sr_4$-type phase were observed for compositions $x = 0.3$, 0.4 and 0.5. To clarify this clearly, the diffraction components from Cu $K\alpha_2$ were striped for comparison. As shown Fig. 1b, small shoulders, corresponding to contribution of the $Sr_4$-type phases, of some characteristic reflections were visually observed. Moreover, a representative Le-bail fitting pattern for $x = 0.5$ presented in Fig. S1† demonstrated that all the reflections could only be well reproduced by a two-phase model fitting. These results indicate that the compositions for $x = 0.3$, 0.4 and 0.5 comprise two phases. More importantly, single-phase for compositions $x = 0.3$, 0.4 and 0.5 was not attainable by neither calcination at elevate temperature nor prolongation of calcination time (Fig. S2†), suggesting the two phases are thermodynamically favorable. Therefore, the compositions for $Ca_{4-x}Sr_xGaNbO_8$ ($x = 0$–4) can be divided into three regions: (i) a single $Ca_4$-type phase region ($x < 0.3$), (ii) a narrow two-phase region contains both $Ca_4$-type and $Sr_4$-type phases ($0.3 \leq x < 0.65$), and (iii) a single $Sr_4$-type phase region ($x \geq 0.65$). We should note that the change of the relative content for the two phases within the two-phase region was slight (Fig. 1b), which is distinctly differ from commonly observed two-phase regions for perovskites *e.g.* the two-phase region observed in $Ba_{3-x}Sr_xZnSb_2O_9$ ($0.3 \leq x \leq 1.0$).[28] Such a difference is attribute to the subtle distinction in crystal structures between $Ca_4$-type and $Sr_4$-type structures, which will be discussed later.

The evolution of normalized lattice parameters against $Sr^{2+}$-content in $Ca_{4-x}Sr_xGaNbO_8$ is presented in Fig. 2, where the linear expansion of the cell volume for single-phase compositions is in good agreement with the PXRD patterns. Interestingly, the lattice parameters for both $Ca_4$-type and $Sr_4$-type phases also showed a linear increase within the two-phase region, which opposite to commonly observed constant lattice parameters for the two phases in the two-phase region. This uncommon phenomenon further corroborated that the co-existence of two phases in $Ca_{4-x}Sr_xGaNbO_8$ is thermodynamically favorable.

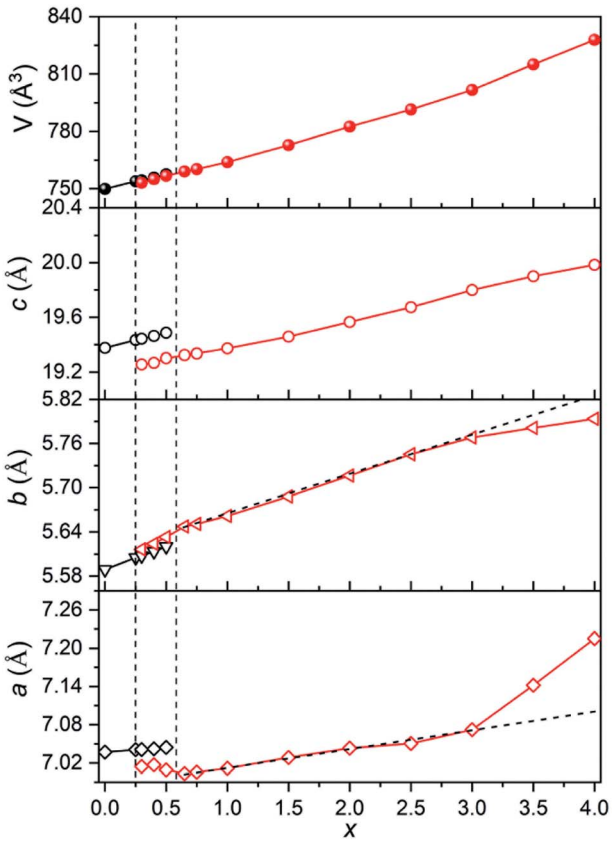


Fig. 2 Plots of lattice parameters against $Sr^{2+}$-content in $Ca_{4-x}Sr_xGaNbO_8$.

## Rietveld refinements

As described above, both $Ca_4$-type and $Sr_4$-type phases adopt oxygen-deficient perovskite-type structure with 1:1:1 triple-cation B-site ordering. Owing to their low structure symmetry ($P2_1/c$), both structures exhibit three distinctly different A-sites (denoted as A1, A2, and A3, respectively), which could be readily discerned through their surrounding environments. As shown in Fig. 3, A1 cation is surrounded by three $B1O_6$ octahedra (B1 represents the B-site occupied by alkali earth cation),

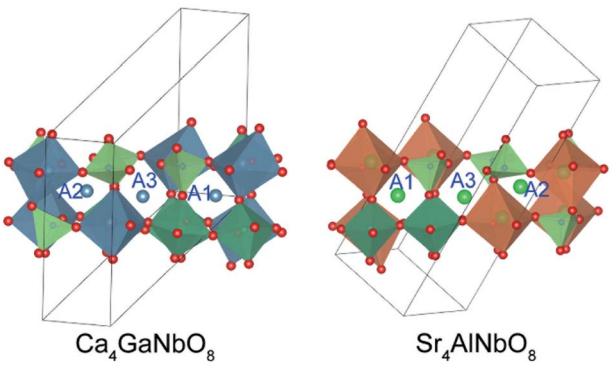


Fig. 3 The surrounding environments for A-site cations in $Ca_4$-type and $Sr_4$-type structures.

four $NbO_6$ octahedra, and one $GaO_4$ tetrahedron; A2 is surrounded by three $B1O_6$ octahedra, one $NbO_6$ octahedron, and four $GaO_4$ tetrahedra; A3 is surrounded by two $B1O_6$ octahedra, three $NbO_6$ octahedra, and three $GaO_4$ tetrahedra. Such difference in surrounding environments for A-site cations results in the A1-site is much larger than A2-and A3-site, suggesting $Sr^{2+}$ is prone to occupy the A1-site at first.

Careful Rietveld refinements against laboratory XRD data were further performed on selected compositions $Ca_{4-x}Sr_xGaNbO_8$ ($x$ = 0, 1, 1.5, 2, 2.5, 3, 3.5 and 4) to get an insight picture of the site occupancy preference for $Sr^{2+}$. The refined structure parameters for $Ca_4GaNbO_8$ is in good agreement with that reported by Yang *et al.* using combined refinements against neutron and synchrotron data (Table S1†). For compositions with $x \geq 1.0$, $Sr_4AlNbO_8$ was used as the starting structure model for Rietveld refinements. At first, an A-site ordered structure model was constructed for preliminary refinements, for instance, $Sr^{2+}$ occupies A1-site exclusively and the remaining two A-sites were occupied by $Ca^{2+}$ in $Ca_3SrGaNbO_8$. The refinement proceeded smoothly with this completely ordered model, resulting in reliable agreement factors ($R_{wp}$ = 7.625%, $R_p$ = 5.592%) and structural parameters. However, some peaks with large discrepancies between the observed and calculated were observed, suggesting the A-site cations are not completely ordering in $Ca_3SrGaNbO_8$. Consequently, the occupancy factor for $Ca^{2+}$ and $Sr^{2+}$ cations at B1-site and three A-sites were refined freely during the subsequent refinements. It turned out that A1-site was dominantly by $Sr^{2+}$, and A2, A3, and B1 sites were mainly occupied by $Ca^{2+}$. Despite the occupancies for $Ca^{2+}$ and $Sr^{2+}$ at four independent sites were refined freely, the refined composition $Ca_{2.92}Sr_{1.08}GaNbO_8$ agrees well with the nominal formula $Ca_3SrGaNbO_8$. Moreover, the reliable factors were improved significantly to $R_{wp}$ = 5.543% and $R_p$ = 4.074%. These results manifest that the $Ca^{2+}$ and $Sr^{2+}$ are partially ordered in $Ca_3SrGaNbO_8$. Rietveld refinements performed on other compositions further demonstrated that all the compositions with mixed A-site cations were partially ordered. We

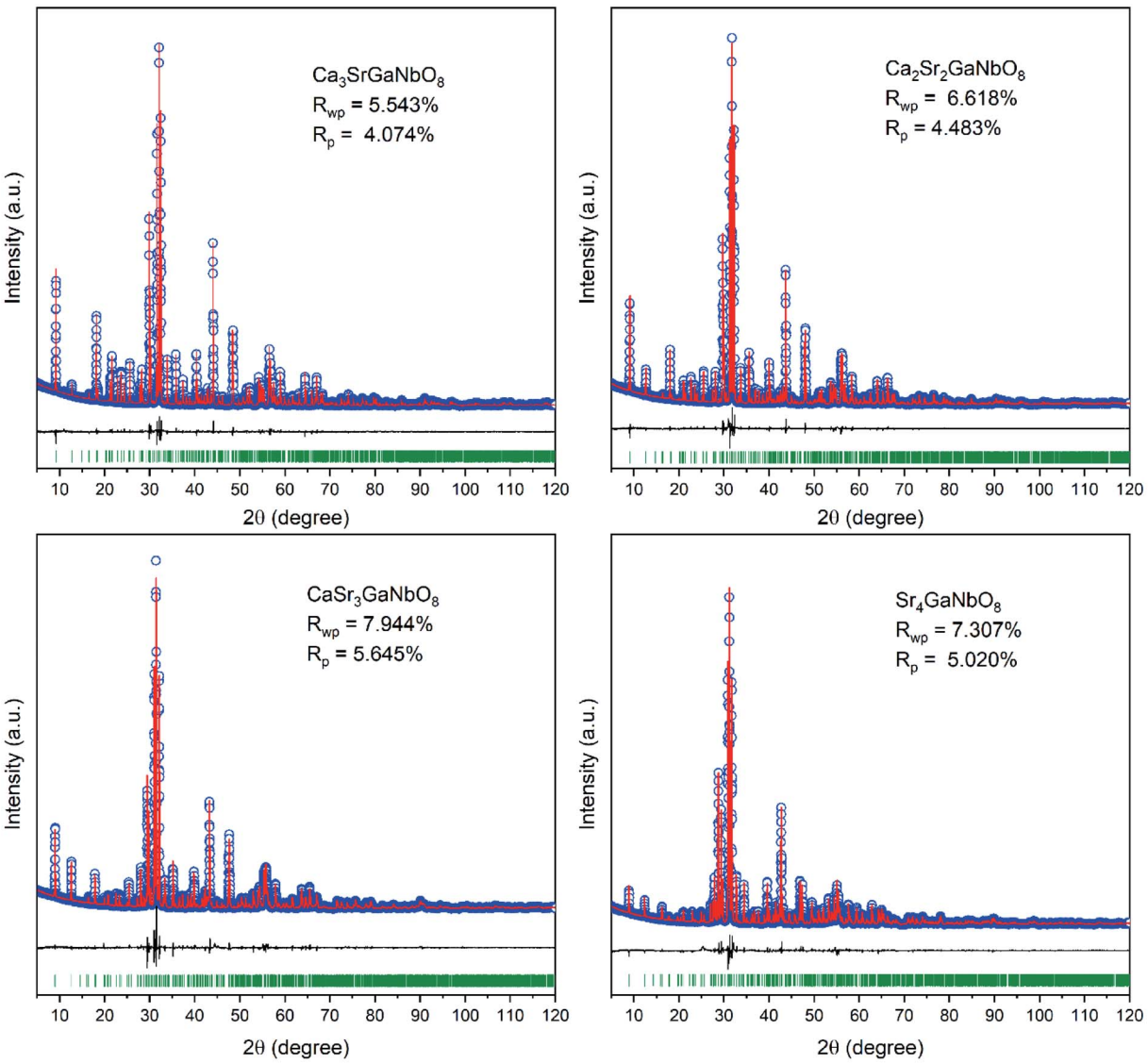


Fig. 4 Rietveld refinement plots of XRD data for $Ca_{4-x}Sr_xGaNbO_8$ ($x$ = 0, 1, 2, 3, 4).

should note that the inversion between A- and B-sites, which is commonly observed in spines,[29] was not considered in $Ca_{4-x}Sr_x$-$GaNbO_8$ because of the large differences in cationic size and coordination environment preference between (Ca, Sr) and (Ga, Nb). The final crystallographic parameters and selected bond lengths for $Ca_{4-x}Sr_xGaNbO_8$ are summarized in Table S1 and S2.† The Rietveld refinement patterns are presented in Fig. 4 and S3.†

### Structure evolution of $Ca_{4-x}Sr_xGaNbO_8$

The refined crystal structures for $Ca_4GaNbO_8$ and $Sr_4GaNbO_8$ are presented in Fig. 5, where both structures view along the same cubic-perovskite direction $[110]_p$. $Ca_4GaNbO_8$ and $Sr_4$-$GaNbO_8$ share the similar structure features with 1:2 layer-ordered hexagonal perovskites *i.e.* $Ca_4Nb_2O_9$, however the structure for $Ca_4GaNbO_8$ and $Sr_4GaNbO_8$ are more complex because there is an another B-site cation ($Ga^{3+}$) and ordered anionic deficiency.[30] As shown in Fig. 5, the removal of oxygen within the $AO_2$ layers creates tetrahedral cavities that could only accommodate smaller $Ga^{3+}$ cations, which resulted in layered stacking sequence of (Ca/Sr)–($Ga_{1/2}Nb_{1/2}$)–($Ga_{1/2}Nb_{1/2}$)–(Ca/Sr) for B-site cations along the closed-packing direction $[111]_p$. Owing to the ordered removal of every other oxygen-only $O_2$ columns within the $AO_2$ layers, $Ga^{3+}$ and $Nb^{5+}$ within ($Ga_{1/2}Nb_{1/2}$)–($Ga_{1/2}Nb_{1/2}$) layers are column ordered along $[110]_p$.

Given the same cationic ordering and oxygen deficient manner, the crystal structures for $Ca_4GaNbO_8$ and $Sr_4GaNbO_8$ seem identical at first glance. Close inspecting the structures revealed that the structural difference between $Ca_4GaNbO_8$ and $Sr_4GaNbO_8$ stems from the distinct orientations of $GaO_4$ tetrahedra along-side of $(Ca/Sr)O_6$ octahedra. As highlighted in Fig. 5, the $GaO_4$ tetrahedra in $Ca_4GaNbO_8$ point to the same direction, however, the $GaO_4$ tetrahedra in $Sr_4GaNbO_8$ point to opposite directions. Such a difference resulted in a doubled cell dimension along $[111]_p$ for $Ca_4GaNbO_8$ in comparison with $Sr_4GaNbO_8$ (see Fig. 5). The structural transformation between two-type structures requires the rearrangement of the orientations of $GaO_4$ tetrahedra along $[110]_p$, which is much more difficult than collective octahedra-tilting observed universally in cubic-type perovskites. Consequently, a narrow two-phase region is observed in $Ca_{4-x}$-$Sr_xGaNbO_8$, and continuous structural transition is usually observed for simple cubic-type perovskites. We thus can speculate that this subtle structural difference in $GaO_4$ orientations is the origin of the formation of the two-phase region in $Ca_{4-x}Sr_xGaNbO_8$.

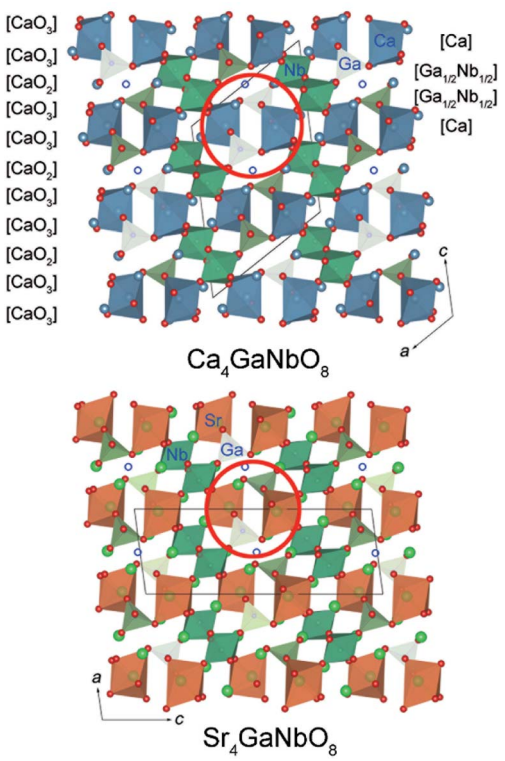


Fig. 5 Comparison of crystal structures for $Ca_4GaNbO_8$ and $Sr_4$-$GaNbO_8$. The open blue circles represent the oxygen-column defects.

The evolution of occupancy factors for $Sr^{2+}$ cations at both A and B sites in $Ca_{4-x}Sr_xGaNbO_8$ is elucidated in Fig. 6a, where a site-selective doping behaviour is observed clearly. In detail, $Sr^{2+}$ prefers to occupy the A1-site, which can be deduced from the sharp increase of occupancy factor to 0.926(6) for $Sr^{2+}$ at A1-site when $x \leq 1.5$, whereas the increase of occupancy factors at A2 and A3 sites are relatively slow. The occupancy factors for $Sr^{2+}$ at A2 and A3 sites show a synchronized increase behaviour in the range of $1.5 \leq x \leq 3.0$, where the $Sr^{2+}$-occupancy at A1 site manifests a slight increase. Further incorporation of $Sr^{2+}$ into $Ca_{4-x}Sr_xGaNbO_8$ lead to a sharp increase of occupancy factor for $Sr^{2+}$ at B1 site when $x \geq 3.0$, whereas a slight increase is observed for $x \leq 3.0$. Such a sharp increase of occupancy of $Sr^{2+}$ at B1-site lead to a significant deviation of the lattice parameters, especially for *a*, from the Vegard's law (see Fig. 2). Given the layered structure nature of $Ca_{4-x}Sr_xGaNbO_8$, when viewed along $[110]_p$, the sharp increase of $Sr^{2+}$-content in B1-site would unambiguously result in a sharp expansion along $[111]_p$, namely *a*-axis of $Sr_4$-type structure (see Fig. 5).

As described above, $Sr^{2+}$ showed a site-selective doping behaviour due to the distinctly large differences in size for A1, A2/A3, and B1 sites. The evolutions of the average ⟨A–O⟩ and ⟨B–O⟩ bond lengths are elucidated in Fig. 6b and c, where the change trends for both ⟨A–O⟩ and ⟨B1–O⟩ bonds are in good agreement with that of occupancy factors. The ⟨Ga–O⟩ and ⟨Nb–O⟩ bond lengths are almost kept in constant at ~1.85 Å and ~2.0 Å, respectively, for all compositions (Fig. 6c). The Ga–O bond lengths in all compounds are in the range of 1.76–1.90 Å, which are comparable with four-coordinated $Ga^{3+}$ in $LaAGa_3O_7$ ($A = Ca^{2+}, Sr^{2+}, Ba^{2+}$).[31–33] Detailed inspection of the Nb–O bonds revealed that the $Nb^{5+}$ exhibits a distorted coordination environment with three Nb–O atomic distances shorter than 2.0 Å and the remaining three bond lengths longer than 2.0 Å (Table S2†), indicating $Nb^{5+}$ displaced from the centre of the octahedral cavity due to the second-order Jahn–Teller (SOJT) effect.[34,35] Though both $Ga^{3+}$ and $Nb^{5+}$ cations can adopt four- and six-fold coordinations, incorporation of $Sr^{2+}$ into A- and B-sites did not lead to anti-site disordering between Ga- and Nb-sites for all compositions, which should unambiguous attribute to their large differences in charge and cationic size.

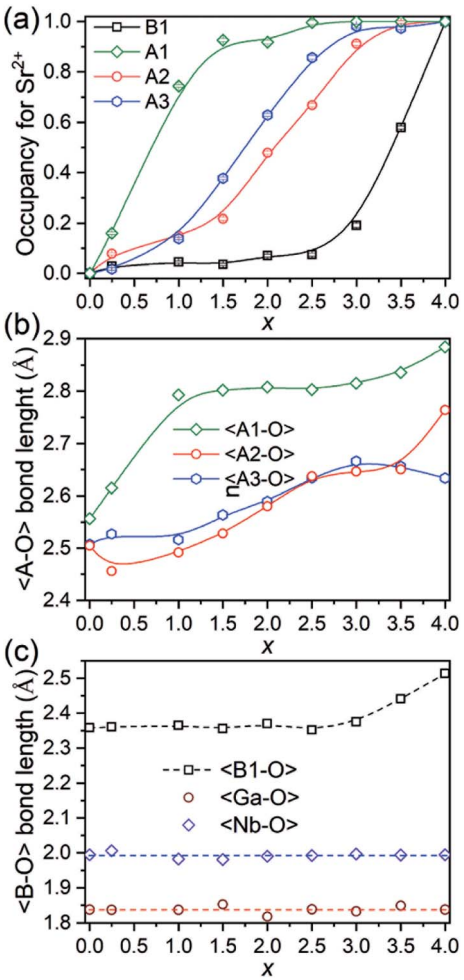


Fig. 6 (a) Plots of occupancy factors for $Sr^{2+}$, (b) average ⟨A–O⟩ bond lengths, and (c) average ⟨B–O⟩ bond length along with $Sr^{2+}$-content in $Ca_{4-x}Sr_xGaNbO_8$.

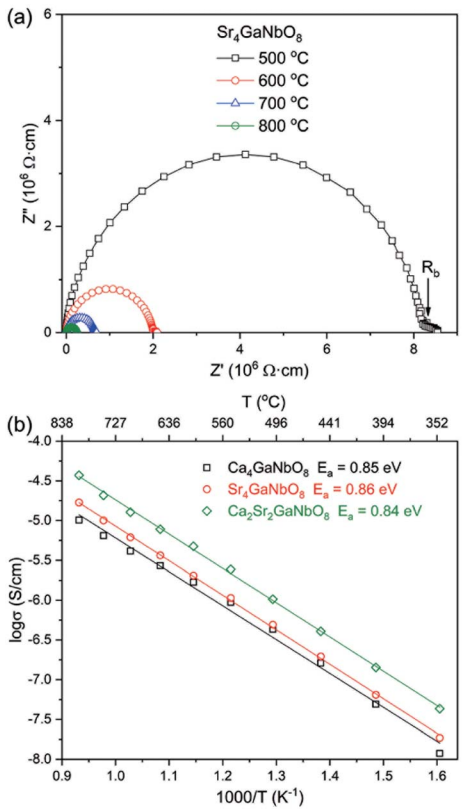


Fig. 7 (a) Typical ac impedance spectra for $Sr_4GaNbO_8$ at different temperatures. (b) Arrhenius plots of bulk conductivities for $Ca_{4-x}Sr_x$-$GaNbO_8$ ($x = 0$, 2, and 4).

It is well known that Raman scattering is sensitive to local structural changes, including cationic ordering, structure symmetry change, and John–Teller distortion.[36] To gain an insight of structural change induced by $Sr^{2+}$-doping, Raman spectra for $Ca_4GaNbO_8$ and $Sr_4GaNbO_8$ were measured. Raman spectra of $Ca_4GaNbO_8$ and $Sr_4GaNbO_8$ show similar features (Fig. S4†), which is consistent with their similar crystal structures. The intensive peaks with wavelength numbers higher than 700 $cm^{-1}$, especially for the strongest peaks with frequency near 800 $cm^{-1}$, are characteristic features for the complex perovskites with B-site ordering.[30] Moreover, the broad band in the middle frequency range of 530–610 $cm^{-1}$ is assigned to be the stretching vibration of Nb–O bonds due to the displacement of $Nb^{5+}$ from the centre of $NbO_6$ octahedra.[37] All these observations from the Raman spectra are coherent with the crystal structures for $Ca_4$-$GaNbO_8$ and $Sr_4GaNbO_8$ obtained by Rietveld refinements.

### Transport properties

Typical AC impedance spectra at different temperatures for $Ca_{4-x}Sr_xGaNbO_8$ ($x = 0$, 2, and 4) are presented in Fig. S5† and 7a, where the well-resolved semicircle in the high frequency rang can be modelled with parallel resistance ($R$) and capacity ($C$) element. This large semicircle is associated with a capacity close to $1 \times 10^{-12}$ F $cm^{-1}$, implying the contribution of bulk response. The absence of inclined-like spike in low frequency range indicates the absence of oxide ionic conductivity. This observation is consistent with the structural features that there are no terminal oxygens, which is capable of immigration at high temperature, boned to only one B-site cation in both $Ca_4$- and $Sr_4$-type structures. Moreover, the oxygen-vacancy ordering is coupled with the B-site cation ordering, which could not be disrupted upon warming. Therefore, the absence of oxide ionic conductivity for $Ca_{4-x}Sr_xGaNbO_8$ is understandable. The plots of conductivities for $Ca_{4-x}Sr_xGaNbO_8$ ($x = 0$, 2, and 4) against temperature is elucidated in Fig. 7b. All the compounds exhibit typical semi-conductive behaviour with comparable bulk conductivities ($10^{-8}$–$10^{-4}$ S $cm^{-1}$) in the measured temperature range. Fitting the $\sigma$–$T$ curves with Arrhenius equation gives active energy of $\sim$ 0.85 eV for all compounds, which in turn corroborated that the B-site cationic ordering is not disrupted by $Sr^{2+}$-to-$Ca^{2+}$ replacement.

## Conclusions

Substitution of $Ca^{2+}$ in $Ca_{4-x}Sr_xGaNbO_8$ with larger $Sr^{2+}$ did not lead to oxygen-vacancy and B-site cation ordering–disordering transition but a $Ca_4$-type ($x < 0.3$) to $Sr_4$-type ($x \geq 0.65$) structure

transition across a narrow two-phase region ($0.3 \leq x < 0.65$). Rietveld refinements revealed that two-type structures possess similar anionic ordering and identical B-site ordering. The structural difference only lies in different orientations of $GaO_4$ tetrahedra, which is responsible for the formation of the narrow two-phase region. In the process of changing the $Ca_4$-phase to $Sr_4$-phase, the $Sr^{2+}$ cations were mainly incorporated into A1-site for $x < 1.5$, and then doped into A2/A3-site for $x < 3$, and finally doped into B1-site ($x \geq 3$). Such site-selective doping behaviour observed in $Ca_{4-x}Sr_xGaNbO_8$ was driven by the distinctly large difference in size for A1, A2/A3, and B1 sites. Incorporation of $Sr^{2+}$ cations into both A and B sites had no influence on the arrangement of $Ga^{3+}$/$Nb^{5+}$ cations and oxygen defects, thus no significant change in electronic properties of $Ca_{4-x}Sr_xGaNbO_8$ was detected.

## Conflicts of interest

There are no conflicts to declare.

## Acknowledgements

This work is financially supported by the National Science Foundation of China (21805020, 21671028, 21771027), Natural Science Foundation of Chongqing (cstc2019jcyj-msxmX0330), Fundamental Research Funds for Central Universities (2019CDQYWL009), Chongqing Special Postdoctoral Science Foundation (XmT2018004), and Postdoctoral Research Foundation of China (2018M643402). We also acknowledge the support of sharing fund of large-scale equipment of Chongqing University (201903150092).

## Notes and references

1 N. Hayashi, T. Yamamoto, H. Kageyama, M. Nishi, Y. Watanabe, T. Kawakami, Y. Matsushita, A. Fujimori and M. Takano, *Angew. Chem., Int. Ed.*, 2011, **50**, 12547–12550.
2 P. Kayser, M. J. Martinez-Lope, J. A. Alonso, M. Retuerto, M. Croft, A. Ignatov and M. T. Fernández-Díaz, *Inorg. Chem.*, 2013, **52**, 11013–11022.
3 R. J. Cava, B. Batlogg, J. J. Krajewski, R. Farrow, L. W. Rupp Jr, A. E. White, K. Short, W. F. Peck and T. Kometani, *Nature*, 1998, **332**, 814–816.
4 R. J. Cava, B. Batlogg, R. B. Van Dover, J. J. Krajewski, J. V. Waszczak, R. M. Fleming, W. F. Peck Jr, L. W. Rupp Jr, P. Marsh, A. C. W. P. James and L. F. Schneemeyer, *Nature*, 1990, **345**, 602–604.
5 Y. Q. Tan, M. Yan and Y. M. Hao, *J. Phys. D: Appl. Phys.*, 2013, **46**, 015303.
6 W. Z. Yang, M. M. Mao, X. Q. Liu and X. M. Chen, *J. Appl. Phys.*, 2010, **107**, 124102.
7 B.-W. Li, M. Osada, T. C. Ozawa and T. Sasaki, *Chem. Mater.*, 2012, **24**, 3111–3113.
8 B. H. Park, B. S. Kang, S. D. Bu, T. W. Noh, J. Lee and W. Jo, *Nature*, 1999, **401**, 682–684.
9 C. A. de Araujo, J. D. Cuchiaro, L. D. McMillan, M. C. Scott and J. F. Scott, *Nature*, 1995, **374**, 627–629.
10 S. Ray, A. Kumar, S. Majumdar, E. V. Sampathkumaran and D. D. Sarma, *J. Phys.: Condens. Matter*, 2001, **13**, 607–616.
11 Y. Krockenberger, K. Mogare, M. Reehuis, M. Tovar, M. Jansen, G. Vaitheeswaran, V. Kanchana, F. Bultmark, A. Delin, F. Wilhelm, A. Rogalev, A. Winkler and L. Alff, *Phys. Rev. B*, 2007, **75**, 020404.
12 G. King and P. M. Woodward, *J. Mater. Chem.*, 2010, **20**, 5785–5796.
13 S. Vasala and M. Karppinen, *Prog. Solid State Chem.*, 2015, **43**, 1–36.
14 H. X. Geng, J. L. Lan, A. Mei, Y. H. Lin and C. W. Nan, *Electrochim. Acta*, 2011, **56**, 3406–3414.
15 K.-Y. Yang, J.-W. Wang and K.-Z. Fung, *J. Alloys Compd.*, 2008, **458**, 415–424.
16 A. Várez, J. Ibarra, A. Rivera, C. León, J. Santamaría, M. A. Laguna, M. L. Sanjuán and J. Sanz, *Chem. Mater.*, 2003, **15**, 225–232.
17 T. Ishihara, H. Matsuda and Y. Takita, *J. Am. Chem. Soc.*, 1994, **116**, 3801–3803.
18 T. Ishihara, J. A. Kilner, M. Honda and Y. Takita, *J. Am. Chem. Soc.*, 1997, **119**, 2747–2748.
19 F. Blanc, D. S. Middlemiss, Z. H. Gan and C. P. Grey, *J. Am. Chem. Soc.*, 2011, **133**, 17662–17672.
20 G. B. Zhang and D. M. Smyth, *Solid State Ionics*, 1995, **82**, 161–172.
21 J. F. Shin, A. Orera, D. C. Apperley and P. R. Slater, *J. Mater. Chem.*, 2011, **21**, 874–879.
22 J. F. Shin, L. Hussey, A. Orera and P. R. Slater, *Chem. Commun.*, 2010, **46**, 4613–4615.
23 R. K. Hona, A. Huq and F. Ramezanipour, *Inorg. Chem.*, 2017, **56**, 14494–14505.
24 T. Yang, J. B. Claridge and M. J. Rosseinsky, *Inorg. Chem.*, 2013, **52**, 3795–3802.
25 A. A. Coelho, *J. Appl. Crystallogr.*, 2018, **51**, 210–218.
26 R. D. Shannon, *Acta Crystallogr., Sect. A: Cryst. Phys., Diffr., Theor. Gen. Crystallogr.*, 1976, **32**, 751.
27 E. Lee and S.-T. Hong, *J. Solid State Chem.*, 2008, **181**, 2930–2934.
28 J. Li, P. F. Jiang, W. L. Gao, R. H. Cong and T. Yang, *Inorg. Chem.*, 2017, **56**, 14335–14344.
29 J.-M. Li, X.-L. Zeng and Z.-A. Xu, *Appl. Phys. Lett.*, 2013, **103**, 232410.
30 I. Levin, J. Y. Chan, R. G. Geyer, J. E. Maslar and T. A. Vanderah, *J. Solid State Chem.*, 2001, **156**, 122–134.
31 J. M. S. Skakle and R. Herd, *Powder Diffr.*, 1999, **14**, 195–202.
32 J. G. Xu, J. H. Wang, X. Tang, X. J. Kuang and M. J. Rosseinsky, *Inorg. Chem.*, 2017, **56**, 6897–6905.
33 C. I. Thomas, X. J. Kuang, Z. Q. Deng, H. J. Niu, J. B. Claridge and M. J. Rosseinsky, *Chem. Mater.*, 2010, **22**, 2510–2516.
34 M. W. Lufaso and P. M. Woodward, *Acta Crystallogr., Sect. B: Struct. Sci.*, 2004, **60**, 10–20.
35 C. J. Howard and M. A. Carpenter, *Acta Crystallogr., Sect. B: Struct. Sci.*, 2010, **66**, 40–50.
36 J.-M. Li, C. H. A. Huan, Y.-W. Du, D. Feng and Z. X. Shen, *Phys. Rev. B*, 2000, **63**, 024416.
37 Y. I. Yuzyuk, E. Gagarina, P. Simon, L. A. Reznitchenko, L. Hennet and D. Thiaudière, *Phys. Rev. B: Condens. Matter Mater. Phys.*, 2004, **69**, 144105.